



19 and non-destructive assessment of tea products, the use of near infrared (NIR) (950-1760 nm)  
20 hyperspectral imaging (HSI) for classification of six different commercial tea products (oolong,  
21 green, yellow, white, black and Pu-erh) is presented. To visualise the HSI data, linear (principal  
22 component analysis (PCA) and multidimensional scaling (MDS)) and non-linear (t-distributed  
23 stochastic neighbour embedding (t-SNE) and isometric mapping (ISOMAP)) data visualisation  
24 methods were compared. t-SNE provided separation of the six commercial tea products into three  
25 groups based on the extent of processing: minimally processed, oxidised and fermented. To  
26 perform the classification of different tea products, a multi-class error-correcting output code  
27 (ECOC) model containing support vector machine (SVM) binary learners was developed. The  
28 classification model was further used to predict classes for pixels in the HSI hypercube to obtain  
29 the classification maps. The SVM-ECOC model provided a classification accuracy of  $97.41 \pm 0.16$   
30 % for the six commercial tea products. The methodology developed provides a means for rapid,  
31 non-destructive, *in situ* testing of tea products, which would be of considerable benefit for process  
32 monitoring, quality control, authenticity and adulteration detection.

33 **Keywords:** Imaging spectroscopy, hypercube, multivariate, data visualisation, neighbourhood  
34 methods

## 35 **1. Introduction**

36 Being the oldest beverage, tea is the most consumed drink in the world (Sang, 2016). Different tea  
37 products exist due to different processes for freshly harvested tea leaves (Lv et al., 2013). There  
38 are six main types of tea products, i.e. oolong, green, yellow, white, black and Pu-erh (Chang,  
39 2015), which differ in terms of processing (see Figure 1). Green, yellow and white tea products  
40 undergo minimal processing, oolong and black tea products have been oxidised while Pu-erh tea

41 has been fermented. The chemical composition of fresh tea (*Camellia sinensis*) leaves is a complex  
42 mixture of caffeine, polyphenols, polysaccharides and nutrients such as protein, amino acids,  
43 lipids, and vitamins (Ruan et al., 2010). Typically, during the processing of fresh tea leaves, such  
44 as oxidation and fermentation, they undergo chemical compositional changes. Free amino acids,  
45 total tea polyphenols, soluble sugars, and caffeine are the four major chemical components that  
46 determine the nature and quality of the final tea products (Ozturk et al., 2016).

47 *Figure 1: Processing steps for different tea products starting from fresh green tea leaves to final*  
48 *products.*

49  
50 Analytical methods used to measure chemical constituents as quality indicators of plant-based  
51 products include high-performance liquid chromatography (HPLC) (Nieh et al., 2009), liquid  
52 chromatography/mass spectrometry (LC/MS) (Tan et al., 2016), gas chromatography/mass  
53 spectrometry (GC/MS) (Jing et al., 2017) and electrochemical systems (Kumar et al., 2016)  
54 (Domínguez et al., 2015). However, these methods have complex sample preparation, are time  
55 consuming, expensive and require a skilled analyst to carry out the experiments (Li et al., 2017).  
56 A non-destructive technique that has been used for analysis of tea processes and quality monitoring  
57 is e-nose (Yaroshenko et al., 2014) (Sharma et al., 2015). E-nose devices usually include an array  
58 of metal oxide sensors which respond to the amount of biochemical volatiles coming into contact  
59 with the corresponding sensor surface to explain the chemical profile (Bhattacharyya et al., 2007).  
60 However, a major disadvantage of e-nose sensors is that they are affected by environmental  
61 conditions such as temperature and humidity, which leads to sensor drift (Baldwin et al., 2011).

62 In recent years, there has been increasing interest in the use of optical spectroscopic techniques for  
63 rapid, non-destructive assessment of food products. NIR spectroscopy is particularly attractive for  
64 this purpose, where changes in the NIR spectral profiles can be correlated to perform qualitative

65 and quantitative analysis of food products (Qu et al., 2015; Fu and Ying, 2016). NIR spectroscopy  
66 has been explored for discrimination (He et al., 2007; Chen et al., 2009), identification (Chen et  
67 al., 2007; Wang et al., 2015) and quality assessment (Panigrahi et al., 2016) of tea products. Also  
68 reported for non-destructive tea analysis are emerging studies utilising imaging techniques for the  
69 identification (Chen et al., 2008), classification (Wang et al., 2015) and for evaluation of sensory  
70 quality (Zhu et al., 2017) of tea products. Integration of spectroscopy and imaging is known as  
71 hyperspectral imaging (HSI) and use of NIR-HSI still seems unexplored in its application to the  
72 analysis of tea products.

73 HSI has been widely used in remote sensing for military applications (Goetz et al., 1985), but it is  
74 now popular in scientific domains such as forensics (Edelman et al., 2012), medical (Lu et al.,  
75 2014), food (Pu et al., 2015), pharmaceutical (Kandpal et al., 2016) and plants (Mishra et al., 2017).  
76 There are reports of the use of HSI for the understanding of different food products such as coffee  
77 (Nansen et al., 2016), tobacco (Garcia-Allende et al., 2008), and seeds of vegetable and fruits  
78 (Shrestha et al., 2016; Kandpal et al., 2016). Some applications of HSI of tea have been reported  
79 but these studies only considered a single variety of tea and measured the visible and very near  
80 infrared (VNIR) range (around 400-1000 nm), which is dominated by the pigments and physical  
81 characteristics of the samples (Zhao et al., 2009; Xie et al., 2015). In comparison to the VNIR  
82 region, the NIR region provides more detailed chemical information such as overtones resulting  
83 from the molecular vibration of O-H, C-H, N-H bonds and their combinations, which can support  
84 a better classification system based on the chemistry of the samples (Mishra et al., 2016).

85 The aim of the present work is to demonstrate the use of NIR (950-1760 nm) HSI for rapid, non-  
86 destructive classification of six different commercial tea products (oolong, green, yellow, white,  
87 black and Pu-erh). The study investigates and compares four different dimensionality reduction

88 techniques (linear and non-linear) to visualise the high dimensional HSI tea data. Furthermore,  
89 multi-class support vector machine (SVM) modelling has been performed to generate spatial  
90 classification maps of tea products.

## 91 **2. Materials and Methods**

### 92 ***2.1. Samples***

93 Six commercial tea samples were obtained from the local market (Glasgow, United Kingdom).  
94 The samples were obtained in airtight sealed packaging and stored at ambient temperature. All  
95 samples of tea were in loose-leaf form. Black, green and white tea were from Vahdam Teas (New  
96 Delhi, India), oolong tea was from Yamamotoyama (California, USA), Pu-erh tea was from The  
97 Tea Makers of London (London, United Kingdom) and yellow tea was of an unspecified Chinese  
98 origin. The six tea products can also be broadly grouped as minimally processed (green, white and  
99 yellow), oxidised (black and oolong tea) and fermented (Pu-erh tea). The samples for each imaging  
100 experiment were transferred on the day of analysis into a black plastic circular container (diameter  
101 = 3.3 cm, depth = 1.3 cm). A different cap was used for each tea to avoid any cross-contamination.

### 102 ***2.2. Hyperspectral imaging measurements***

103 Imaging was performed with a push-broom line scan HSI camera (*Model name*: RedEye 1.7) from  
104 INNO-SPEC (Nurnberg, Germany). The camera has an InGaAs sensor and generates a spatial map  
105 of 320 x 256 pixels in the spectral range of 950 - 1760 nm. The pixel size was 30 x 30  $\mu\text{m}^2$  and  
106 the spectral resolution was 3.2 nm. The camera communicated with the computer via a gigabit  
107 Ethernet connection. The lighting was provided by two halogen light sources 50 W each and the  
108 integration time used was 300 ms. Imaging was performed by placing the samples over the

109 translation stage which was controlled by an independent stage motor connected to the computer  
110 system (Zolix TSA 200 BF). The speed of the translation stage was optimised before image  
111 acquisition to avoid any distortion in the shape of the image arising from the overlapping of the  
112 spectral information in the adjacent pixels. The image acquisition and management of settings  
113 (integration time) were performed using the software interface called SiCAP provided with the  
114 camera by INNO-SPEC. Images were first acquired of six different tea samples placed adjacent to  
115 each other in their respective sample containers in the field of view of the camera. An image was  
116 then acquired of black, Pu-erh and oolong teas where each tea occupied approximately a third of  
117 the volume of the sample container; the teas were not physically mixed. Finally, equal proportions  
118 of all six tea samples were mixed, by manually shaking the different tea products in a container,  
119 and an image of the mixture was acquired. One image was acquired of each sample, with each  
120 image comprising more than 2000 pixels (spectra) for the individual tea samples and more than  
121 11200 pixels for the samples containing more than one type of tea. An illustration of the HSI setup  
122 configured for imaging of tea samples can be found in Figure 2.

123 *Figure 2: Illustrative diagram for the hyperspectral imaging setup used to acquire the images of tea*  
124 *samples.*

## 125 **2.3. Data analysis**

### 126 **2.3.1. Pre-processing of HSI data**

127 The data cubes not only contain information about the samples imaged but also consist of different  
128 unwanted influences in signal resulting from factors such as illumination intensity, the detector  
129 sensitivity and transmission properties of the optics. The effects resulting from these factors are  
130 both wavelength dependent and independent. To correct for these effects, radiometric calibration

131 was performed using dark and white reference images acquired along with the samples. The  
132 correction was performed for every pixel in the HS image according to equation 1:

$$I_{R(i,j)} = \frac{I_{raw(i,j)} - I_{dark(i,j)}}{I_{white(i,j)} - I_{dark(i,j)}} \quad (1)$$

133

134 where,  $I_R$  is the calibrated reflectance image,  $I_{raw}$  is the raw intensity image measured from the test  
135 sample,  $I_{dark}$  is the intensity of the dark response,  $I_{white}$  is the intensity for the uniform white  
136 reference and  $i$  and  $j$  were spatial coordinates over the image.

137 Often, the radiometric correction is sufficient to remove the effects of illumination inhomogeneity  
138 from the spectral data, however, when the sample surfaces are not uniform, as in the case of  
139 samples of loose tea leaves, the light scattering during diffuse reflection causes additive and  
140 multiplicative effects (Mishra et al., 2016). These scattering effects lead to baseline shifts in the  
141 spectrum and variation in the global intensity, which is again dependent on the wavelength.  
142 Standard normal variate (SNV) is a very common technique used in NIR spectroscopy to remove  
143 these effects (Barnes et al., 1989). In SNV, the mean and standard deviation of each spectrum for  
144 each pixel are calculated, the mean is subtracted, and the standard deviation is used to normalise  
145 the difference. This transformation normalises each spectrum to zero mean and unit standard  
146 deviation. Before applying the SNV transform, the spectral range was reduced from 950 - 1760  
147 nm to 967 nm - 1700 nm, to remove the noisy regions at the edges of the spectral range, and  
148 converted to absorbance. Further, the spectral absorbance profiles were smoothed with a Savitzky-  
149 Golay filter (15-point width and second order polynomial) (Savitzky and Golay, 1964). The *savgol*  
150 and *snv* functions from PLS toolbox (version 8.11, Eigenvector Research Inc., USA) were used.  
151 All visualisation and classification analysis was performed on the pre-processed spectra. The pre-

152 processed pure spectra of six pure tea samples were extracted using Matlab's (R2016b,  
153 Mathworks, USA) *roipoly* function. The *roipoly* function provides a graphical user interface in  
154 Matlab to extract the information from each image over the manually selected locations.

### 155 **2.3.2. Principal Component Analysis**

156 Principal component analysis (PCA) introduced by Pearson in 1901 belongs to the family of linear  
157 methods for visualising high dimension data (Wold et al., 1987). In PCA, a set of observations  
158 containing correlated variables is orthogonally transformed to linearly uncorrelated variables  
159 defined as principal components (PCs). In PCA, the transformation is performed to retain the major  
160 amount of variability in the dataset.

161 The PCA decomposition model for a given observation data matrix  $X$  can be understood as  
162 equation 2:

$$163 \quad \mathbf{X} = \mathbf{T}\mathbf{W}^T \quad (2)$$

164 where  $T$  is the score in the lower dimension explained by the number of PCs specified and  $W$  is a  
165  $p \times p$  ( $p$  denotes number of variables) matrix whose columns are the eigenvectors of  $X^T X$ .

166 In the case of dimensionality reduction, the aim is to preserve the maximum amount of meaningful  
167 variation present in the dataset. The extracted PCs define a new orthonormal basis set which can  
168 be used to transform the data from a high dimension space to the lower space explained by the  
169 PCs. PCA from a dimensionality reduction perspective can be understood as minimising the  
170 squared reconstruction error as given in equation 3.



171 
$$\min \|TW^T - T_r W_r^T\|^2 \quad (3)$$

172 where,  $TW$  and  $T_r W_r$  are the reconstructed original dataset in higher and lower dimensional space  
 173 respectively. Minimisation of the reconstruction error results in the maximisation of the  
 174 information that was present in the higher dimensional space when defined in the lower  
 175 dimensional space given by the significant number of PCs. To interpret the data in two or three  
 176 dimensional plots, the respective PCs can be selected and used for transformation to the orthogonal  
 177 axes represented by the PCs. Transformation from a higher dimension to a lower dimension can  
 178 be performed as in equation 4.

179 
$$\hat{X}_r = XW \quad (4)$$

180 **2.3.3. Multi-Dimensional Scaling**

181 Multi-dimensional scaling (MDS) is a linear method for visualising high dimensional data (Cox et  
 182 al., 2000). MDS performs a transformation by preserving the between object distances from the  
 183 higher dimension to lower dimension. The MDS utilises calculation of the Euclidean distances for  
 184 each data point in the multidimensional space to capture the pattern. The distances are defined as  
 185 a symmetric distance matrix ( $D$ ). MDS attempts to find data points in a specified (d-dimensional)  
 186 space such that the Euclidean distance between data points ( $\hat{D}$ ) is similar to the distance in higher  
 187 dimensional space. The minimisation function can be understood as equation 5:

188 
$$\min \sum_i \sum_j \|d_{ij} - \hat{d}_{ij}\|^2 \quad (5)$$

189 where,  $D = d_{ij} = \|x_i - x_j\|^2$  and  $\hat{D} = d_{ij} = \|y_i - y_j\|^2$  explaining the Euclidean distance between  
190 points in high  $(x_i, x_j)$  and low dimensional space  $(y_i, y_j)$ , respectively.  $i, j$  denotes specific position  
191 of point.

#### 192 **2.3.4. Isometric Mapping**

193 Isometric mapping (ISOMAP) belongs to the family of non-linear techniques for visualising high  
194 dimensional data (Tenenbaum, 1998; Balasubramanian and Schwartz, 2002). ISOMAP can be  
195 understood as a generalised non-linear form of MDS which utilises the geodesic space accounting  
196 for the non-linearity in the high dimensional data manifold. The geodesic distance is defined as  
197 the shortest distance between two data points on a curved surface of a non-linear manifold. As a  
198 first step, ISOMAP approximates a neighbourhood graph by identifying  $k$  nearest neighbours  
199 (kNNs) or selecting neighbourhood data points based on any other condition for every data points.  
200 The geodesic distance is then approximated for all the pairs of data points on the neighbourhood  
201 graph. Finally, the distance data obtained from the graph is embedded to a lower dimension  
202 Euclidean space using MDS as shown in equation (6).

$$\min \sum_i \sum_j \|D_G - D_E\|^2 \quad (6)$$

203

204 where,  $D_G$  and  $D_E$  explaining the geodesic and Euclidean distance between points in high and low  
205 dimensional space, respectively.

206

#### 207 **2.3.5. $t$ -Distributed Stochastic Neighbour Embedding**

208 t-distributed stochastic neighbour embedding (t-SNE) is a non-linear technique used to visualise  
 209 high dimensional data in two or three dimensional scatter plots (Maaten and Hinton, 2008). The  
 210 main objective of t-SNE is to model the similar points using nearby points (small pairwise  
 211 distance) and the dissimilar points using distant points (large pairwise distances). As a first step,  
 212 to represent the similarity, the t-SNE converts high-dimensional Euclidean distances between data  
 213 points into conditional probabilities using a Gaussian distribution. The joint probability for a data  
 214 point  $\mathbf{x}_j$  to  $\mathbf{x}_i$  can be calculated with equation (7):

$$p_{ji} = \frac{\exp(-\|\mathbf{x}_i - \mathbf{x}_j\|^2 / 2\sigma_i^2)}{\sum_k \sum_{k \neq l} \exp(-\|\mathbf{x}_k - \mathbf{x}_l\|^2 / 2\sigma_i^2)}, \quad (7)$$

215  
 216 The conditional probability represents the probability that  $\mathbf{x}_i$  will pick  $\mathbf{x}_j$  as a neighbour based on  
 217 the proportion of probability density under a Gaussian centred at  $\mathbf{x}_i$ . If the points are near then the  
 218 value of  $p_{ij}$  will be higher compare to the points far away. Furthermore, the conditional  
 219 probabilities are symmetrised to reduce the effects of outliers by setting (8):

$$p_{ij} = \frac{p_{ji} + p_{ij}}{2N} \quad (8)$$

220  
 221 To represent joint probabilities in the low dimensional map  $q_{ij}$ , t-SNE utilises a heavy tailed  
 222 Student t-distribution. The benefit of using a heavy tailed distribution is that it makes the joint  
 223 probabilities invariant to changes in the scale of the map. The joint probabilities  $q_{ij}$  can be  
 224 estimated by (9):

$$q_{ij} = \frac{(1 + \|y_i - y_j\|^2)^{-1}}{\sum_k \sum_{k \neq l} (1 + \|y_k - y_l\|^2)^{-1}}, \quad (9)$$

225

226 Finally, the t-SNE minimises a single Kullback-Leibler (*KL*) divergence between a joint  
 227 probability distribution,  $P$ , in the high-dimensional space and a joint probability distribution,  $Q$ , in  
 228 the low-dimensional space as can be understood from equation (10):

$$KL(P||Q) = \sum_i \sum_j p_{ij} \log \frac{p_{ij}}{q_{ij}} \quad (10)$$

229

230 The minimisation of the *KL* divergence is performed using a gradient descent algorithm with  
 231 respect to the locations of the points in the map  $y_i$ .

232 All the data visualisation methods (PCA, MDS, ISOMAP and t-SNE) were implemented in Matlab  
 233 using the Toolbox for Dimensionality Reduction (<https://lvdmaaten.github.io/drtoolbox/>) (Maaten  
 234 et al., 2009; Maaten and Hinton, 2008). The Mahalanobis distance (Mahalanobis, 1936) was used  
 235 to assess the separation of the clusters identified with the different data visualisation methods.

### 236 **2.3.6. Support vector machines for multi-class classification**

237 Support vector machines (SVMs) are supervised non-probabilistic learning models which utilise  
 238 hyperplanes to define the decision boundaries for performing classification (Vapnik and Vapnik,  
 239 1998). The SVM algorithms are usually developed to perform a binary classification, however,  
 240 SVM can be used for multi-class classification problems by utilising several independent binary  
 241 classifiers. This can be performed by combining it with ensemble methods such as error correcting  
 242 output codes (ECOC). The ECOC deals with the multi-class classification problem by converting

243 it into several independent binary classification problems. A wide range of applications of SVM  
244 to process HS images can be seen (García Allende et al., 2008) (Mountrakis et al., 2011).

245 In the present work, the ECOC-SVM algorithm available in Matlab's Statistics and Machine  
246 Learning Toolbox (R2016b) was implemented to perform the classification utilising the  
247 classification learner application. ECOC-SVM uses a one-versus-all coding design, in which for  
248 each binary learner one class is assigned a positive value and all others are assigned negative  
249 values. To map the data to the higher dimension, a radial basis function (RBF) kernel (scale  
250 parameter=10) was used. The RBF kernel has the benefit of non-linearly mapping the sample to  
251 the higher dimensional space for dealing with a non-linear relationship between observation and  
252 classes. For every pure tea sample, spectra (967 - 1700 nm) were extracted from 200 pixels, which  
253 were selected at random from the image collected, leading to 1200 spectra in total for calibration  
254 of the classification model. Validation of the model was performed with a 10-fold cross-validation  
255 method. Furthermore, to have confidence in the model accuracy, the model was recalibrated with  
256 1200 iterations and the mean and standard deviation were noted. The trained classifier was further  
257 used to generate the classification maps of the HS images. The HSI cubes were first unfolded from  
258 a 3D map ( $n \times p \times k$ ) to a 2D matrix ( $np \times k$ ) and then the class of every row of the matrix  
259 (representing the pixel) was predicted, where n, p, k defined the x, y and z dimension of data. After  
260 prediction, the matrix ( $np \times 1$ ) was reshaped to the original image dimension ( $n \times p$ ).

## 261 **3. Results**

### 262 *3.1. Spectral profiles of tea samples*

263

264 *Figure 3: Absorbance spectra of pure tea samples of yellow, oolong, green, black, white and Pu-*  
265 *erh. (a). Mean absorbance spectra ( $n = 200$ ). (b) Mean spectra after pre-processing (SNV and*  
266 *Savitzky- Golay smoothing), and (c) standard deviation of the absorbance spectra and spectra*  
267 *after pre- processing. The vertical green lines denote the positions of the main peaks.*

268

269 Figure 3 presents the spectral profiles of individual tea samples. Figure 3(a) presents the mean  
270 absorbance spectra calculated from the 200 spectra extracted for each of the six tea samples  
271 (yellow, oolong, green, black, white and Pu-erh), Figure 3(b) presents the mean spectra after pre-  
272 processing with Savitzky-Golay filtering followed by SNV, and Figure 3(c) presents the standard  
273 deviation of the spectra before and after pre-processing. From Figure 3(a), it can be seen that the  
274 absorbance spectra of different tea samples contain scattering effects leading to baseline shifts.  
275 These effects can also be seen in the standard deviation plot in Figure 3(c) for the absorbance  
276 spectra (red), where the standard deviation over the entire spectral range is approximately constant.  
277 These scattering effects can bias modelling of the data, therefore, they were removed via pre-  
278 processing. In Figure 3(b), it can be seen that after pre-processing, differences in spectra at various  
279 wavelengths have emerged, and so spectral differences corresponding to different teas can be  
280 noted. Scattering effects arise in the imaging experiments as the inhomogeneity in the size of the  
281 loose leaves does not get compensated for by the flat surface of the white reflectance standard used  
282 for radiometric calibration.

283 In Figure 3(c), it can be noted that the pre-processing reveals the spectral variation arising from  
284 differences in the tea, which was previously dominated by the effects of light scattering. In Figure  
285 3(b), various peaks (depicted by the green vertical lines) can be identified at representative  
286 wavelengths. In previous works, the peaks at 1131, 1654 and 1666 nm were found to be

287 representative of the total tea polyphenols (Chen et al., 2006; Bian et al., 2010; Bian et al., 2013),  
288 1361 nm is representative of moisture content (Panigrahi et al., 2016), 1093-1121 nm for  
289 thearubigin components of TRS1 (Panigrahi et al., 2016), 1492 nm corresponds to free amino acids  
290 (Bian et al., 2010), 1176 nm is a second overtone C-H (Tan et al., 2012) and 1390 nm for the CH<sub>2</sub>  
291 overtone (Lee et al., 2014).

### 292 **3.2. Visualising high dimensional data**

293

294 *Figure 4: 2-Dimensional scatter plots for visualising high dimensional tea data. (a). Principal Component*  
295 *Analysis (PCA), (b). Multidimensional Scaling (MDS), (c). Isometric Mapping (ISOMAP), and (d). t-*  
296 *distributed Stochastic Neighbour Embedding (t-SNE). In all the plots, the first dimension is represented in*  
297 *the x-axis and the second in the y-axis, and the six tea products are coloured as follows: Pu-erh (pink),*  
298 *black (sky blue), oolong (yellow), green (green), white (blue) and yellow (red).*

299 To visualise the high dimensional data in the lower dimension, the 256-dimensional HSI data were  
300 transformed to 2-dimensional plots using PCA, MDS, ISOMAP and t-SNE as shown in Figure 4.  
301 It can be seen clearly in Figure 4 that the t-SNE (Figure 4(d)) outperforms PCA, MDS and  
302 ISOMAP (Figures 4(a), 4(b) and 4(c), respectively) regarding identification of the maximum  
303 number of separate clusters. These separate clusters correspond to different tea products and their  
304 representation as separate clusters in the plots signifies that the visualisation method is able to  
305 preserve the structure of the data on transformation from a high dimensional space to a lower  
306 dimensional space. In general, all the methods were able to separate the Pu-erh tea (pink) from all  
307 other tea samples. The reason for this can be seen in Figure 3(b) where Pu-erh tea (sky blue) has a  
308 very different spectral signature compared to the other tea samples. This is likely to be because the

309 Pu-erh tea undergoes very different processing, which includes microbial fermentation of sun dried  
310 leaves (Lv et al., 2013), compared to the other teas.

311 It can be seen in Figure 4((a), (b) and (c)) that with the exception of Pu-erh tea, all other types of  
312 tea samples are mixed and their clear distinction is not possible. In comparison, black and oolong  
313 tea are identified as separate clusters with t-SNE. However, while t-SNE was not able to separate  
314 the green, yellow and white tea, it still provided better separation of these three teas as shown in  
315 Figure 4(d). Green, yellow and white teas appear in the same cluster as they have similar spectral  
316 signatures (see Figure 3(b)). This may arise from the fact that these teas are most similar in terms  
317 of processing conditions; they are subjected to either limited or no oxidation. In comparison,  
318 oolong and black teas undergo oxidation during their manufacturing. This may be why these two  
319 teas lie in two adjacent clusters that are far away from the cluster containing green, yellow and  
320 white teas. However, further information is required to identify the exact source of the spectral  
321 differences observed.

322

323 *Figure 5: Mahalanobis distances between the three different cluster groups obtained using PCA (dark-*  
324 *blue), MDS (sky-blue), ISOMAP (light- green) and t-SNE (yellow).*

325 To assess further the separation of clusters with each method, the Mahalanobis distance between  
326 the clusters was calculated. Figure 5 presents the Mahalanobis distance estimated for the three  
327 major clusters identified in Figure 4. The three major cluster can be understood as the group of  
328 minimally processed tea products available on the market (denoted the green group), the teas  
329 subjected to oxidation (oxidised group) and those that have been subjected to microbial fermented  
330 (fermented group). The x-axis in Figure 5 presents the pairwise groups used for estimating the



331 distance and the y-axis gives the respective Mahalanobis distance obtained from the different data  
332 visualisation methods. It can be seen that the t-SNE (yellow) was superior to all other methods  
333 followed by the ISOMAP (light green), and then PCA (dark blue) and MDS (sky blue) for  
334 separating all three groups in the data-visualisation plots.

335 From a statistical perspective, a better visualisation of separate clusters corresponding to different  
336 tea products with t-SNE could be due to its ability to capture the non-linearity present in the data  
337 set and consideration of neighbourhood information. This supports the modelling of both distant  
338 and nearby points (Maaten and Hinton, 2008). Often, in high dimensional space when the data lies  
339 near, or in a non-linear manifold, linear methods like PCA and MDS fail to preserve the structure  
340 of data in the lower dimension space. This is because with linear methods like PCA and MDS, the  
341 aim is to keep the distant object far apart; no consideration is given to utilising the information  
342 about the neighbouring data points (Maaten et al., 2009).

343 It can be seen in Figure 4(c) that ISOMAP provides a little insight on differences in the classes  
344 belonging to black and oolong teas compared to what was achieved with PCA (Figure 4(a)) and  
345 MDS (Figure 4(b)). However, ISOMAP was not able to provide a clear separation of the two teas  
346 as was obtained with t-SNE. A reason for the poor performance of ISOMAP compared to t-SNE  
347 could be due to its weakness in dealing with the holes and non-convex nature of the data manifold  
348 in the higher dimension (Tenenbaum, 1998). Another important weakness of ISOMAP is its  
349 topological instability, which leads to a short-circuiting problem in the neighbourhood graph and  
350 results in its poor performance (Balasubramanian and Schwartz, 2002).

### 351 ***3.3. Support vector machine classification***

352

353 *Figure 6: (a) Greyscale image constructed from the spectral plane extracted from the hypercube at 1424*  
354 *nm, (b) Classification maps obtained from the application of the ECOC-SVM model. From left to right the*  
355 *samples can be understood as yellow (dark blue), oolong (light blue), green (cyan), black (light green),*  
356 *white (orange) and Pu-erh (yellow). (c) Histograms showing the proportion of pixels attributed to the*  
357 *different tea products for the classification maps in (b).*

358 The results from the application of the ECOC-SVM multi-class classification model are presented  
359 as classification maps in Figures 6 and 7. Figure 6(b) presents the classification maps of pure tea  
360 samples, from left to right, the samples can be understood as yellow, oolong, green, black, white  
361 and Pu-erh. For comparison, a greyscale image was also produced (Figure 6(a)) using the spectral  
362 plane corresponding to 1424 nm; this wavelength was selected merely to allow visualisation of the  
363 data hypercube. It can be seen from Figure 6(b) that all six teas were classified into their respective  
364 individual classes. However, there are some pixels that were misclassified; Figure 6(c) shows the  
365 proportion of pixels attributed to the different tea products for the classification maps in Figure  
366 6(b). The misclassification was most dominant at the edges owing to signal from the circular  
367 sample container; such pixels (approximately 20%) were misclassified as Pu-erh. When these  
368 pixels were excluded, an overall accuracy of  $97.41 \pm 0.16$  % was obtained for cross-validated  
369 samples using 1200 iterations.

370 Apart from the edges, a reason for the misclassification between different teas can be attributed to  
371 their spectral similarity. When visualising the data with t-SNE (see Figure 4(d)), green, white and  
372 yellow tea were found to be lying near in the same cluster, and black and oolong were near to each  
373 other due to their spectral similarity. Hence, the classification map for the yellow tea (dark blue)  
374 has some misclassified pixels that have been attributed to either white (orange) or green tea (cyan).  
375 For black and oolong teas, it can be noted that there are some pixels in the classification map for

376 black tea (light green) that were misclassified as oolong (light blue class) and vice-versa. Another  
377 possible reason for misclassification could arise from the purity of the tea; for example, a  
378 minimally processed tea (e.g. white) may contain small amounts of oxidised product (e.g. black  
379 tea).

380

381 *Figure 7: (a). Greyscale image at 1424 nm for the sample comprising oolong, black and Pu-erh tea, (b).*  
382 *The classification map for the sample comprising oolong, black and Pu-erh tea, (c). Pie chart representing*  
383 *the proportion of pixels belonging to a particular class for the classification map presented in (b), (d).*  
384 *Greyscale image at 1424 nm for a sample containing a mixture of all teas, (e). The classification map for*  
385 *a sample containing a mixture of all teas, and (f) Pie chart representing the proportion of pixels belonging*  
386 *to a particular class for the classification map presented in (e).*

387 Figure 7 presents the classification maps for the HS images acquired for samples comprising  
388 mixtures of teas. This analysis was performed to assess the feasibility of using the methodology  
389 developed to classify different tea samples when more than one tea is present. Figure 7(a) presents  
390 the spectral plane corresponding to 1424 nm for a sample containing oolong, black and Pu-erh teas  
391 (not mixed) in roughly equal portions. These three teas were selected as there is an oxidation stage  
392 in their manufacturing. The location of the different teas in Figure 7(a) can be identified with the  
393 red markers. As can be seen from Figure 7(b), the model provided a clear classification of the three  
394 teas into their respective classes. However, some misclassification can be seen at the interface  
395 between different types of teas; individual pixels will detect the presence of more than one type of  
396 tea at these locations. Furthermore, Figure 7(c) provides insight into the proportion of pixels  
397 belonging to each class. It can be seen that the pie chart is mainly dominated by the proportion of  
398 oolong, black and Pu-erh tea and contains a very small portion (<1 %) of pixels classified as green,

399 white and yellow.

400 The methodology developed was also tested for a mixture of all six tea samples. The result for  
401 classification of the sample containing a mixture of all six types of tea is presented in Figure 7(e).  
402 The classification map shown in figure 7(e) can be interpreted in conjunction with the pie chart  
403 (Figure 7(f)) representing the proportion of pixels classified belonging to different classes. The pie  
404 chart shows that the presence of all the classes can be detected with the classification model and  
405 the portion of each type of tea ranged from 10 – 26%. However, it was not possible to validate the  
406 classification result of the mixture image because it is not known if the sample was a homogenous  
407 mixture of the six types of teas and hence, the exact composition of the upper surface of the sample  
408 is unknown. In addition, there may be some misclassification of pixels that detect more than one  
409 type of tea.

#### 410 **4. Conclusions**

411 NIR HSI has been used to classify six different types of commercial tea samples. Before any data  
412 modelling, the spectral imaging data from tea products should be pre-processed to reduce the  
413 effects of light scattering arising from the inhomogeneous and uneven leaf surface. Four different  
414 types of linear and non-linear dimensionality reduction methods were compared for visualisation  
415 of imaging data. The non-linear method, t-SNE, gave better separation of the different tea products  
416 than classical linear techniques such as PCA and MDS. This is because t-SNE uses information  
417 from neighbouring data points in the high dimensional space to preserve the structure in the low  
418 dimensional representation. It was possible to classify the tea according to product type using a  
419 ECOC-SVM multi-class classification model constructed using the NIR HSI data. Therefore, NIR  
420 HSI in conjunction with machine learning could be a potential tool for classification of different

421 types of tea products. The source of spectral differences is assumed to arise from the different  
422 processing steps that are involved in the manufacture of various types of tea. However, there could  
423 be other sources, e.g. geographical, that contribute to spectral differences and hence, this requires  
424 further investigation.

## 425 **5. Acknowledgments**

426 This work has received funding from the European Union's Horizon 2020 research and innovation  
427 programme named 'MODLIFE' (Advancing Modelling for Process-Product Innovation,  
428 Optimization, Monitoring and Control in Life Science Industries) under the Marie Skłodowska-  
429 Curie grant agreement number 675251.

430

## 431 **6. References**

432 Balasubramanian, M., Schwartz, E.L., 2002. The Isomap Algorithm and Topological  
433 Stability. *Science* (80). 295, 7 LP –7.

434 Baldwin, E.A., Bai, J., Plotto, A., Dea, S., 2011. Electronic Noses and Tongues:  
435 Applications for the Food and Pharmaceutical Industries. *Sensors* (Basel). 11(5), 4744-  
436 4766. <https://doi.org/10.3390/s110504744>

437 Barnes, R.J., Dhanoa, M.S., Lister, S.J., 1989. Standard Normal Variate Transformation  
438 and De-Trending of Near-Infrared Diffuse Reflectance Spectra. *Appl. Spectrosc.* 43,  
439 772–777. <https://doi.org/10.1366/0003702894202201>

440           Bhattacharyya, N., Seth, S., Tudu, B., Tamuly, P., Jana, A., Ghosh, D., Bandyopadhyay,  
441           R., Bhuyan, M., 2007. Monitoring of black tea fermentation process using electronic  
442           nose. *J. Food Eng.* 80, 1146–1156.

443           <https://doi.org/https://doi.org/10.1016/j.jfoodeng.2006.09.006>

444           Bian, B.M., Skidmore, A.K., Schlerf, M., Fei, T., Liu, Y.F., Wang, T., 2010. Reflectance  
445           spectroscopy of biochemical components as indicators of tea, *Camellia Sinensis*, quality  
446           76, 1385–1392.

447           Bian, M., Skidmore, A.K., Schlerf, M., Wang, T., Liu, Y., Zeng, R., Fei, T., 2013.  
448           Predicting foliar biochemistry of tea (*Camellia sinensis*) using reflectance spectra  
449           measured at powder, leaf and canopy levels. *ISPRS J. Photogramm. Remote Sens.* 78,  
450           148–156. <https://doi.org/https://doi.org/10.1016/j.isprsjprs.2013.02.002>

451           Chang, K, 2015. World tea production and trade: current and future development, Food  
452           and Agriculture Organisation (FAO), United Nations (UN), Rome.

453           <http://www.fao.org/3/a-i4480e.pdf> (last accessed: 14 September 2017)

454           Chen, Q., Zhao, J., Cai, J., 2008. Identification of Tea Varieties Using Computer Vision.  
455           *Transactions of the ASABE.* 51(2), 623-628. <https://doi.org/10.13031/2013.24363>

456           Chen, Q., Zhao, J., Fang, C.H., Wang, D., 2007. Feasibility study on identification of  
457           green, black and Oolong teas using near-infrared reflectance spectroscopy based on  
458           support vector machine (SVM). *Spectrochim. Acta Part A Mol. Biomol. Spectrosc.* 66,  
459           568–574. <https://doi.org/https://doi.org/10.1016/j.saa.2006.03.038>

460 Chen, Q., Zhao, J., Huang, X., Zhang, H., Liu, M., 2006. Simultaneous determination of  
461 total polyphenols and caffeine contents of green tea by near-infrared reflectance  
462 spectroscopy. *Microchem. J.* 83, 42–47.  
463 <https://doi.org/http://dx.doi.org/10.1016/j.microc.2006.01.023>

464 Chen, Q., Zhao, J., Lin, H., 2009. Study on discrimination of Roast green tea (*Camellia*  
465 *sinensis* L.) according to geographical origin by FT-NIR spectroscopy and supervised  
466 pattern recognition. *Spectrochim. Acta Part A Mol. Biomol. Spectrosc.* 72, 845–850.  
467 <https://doi.org/http://dx.doi.org/10.1016/j.saa.2008.12.002>

468 Cox, T.F., Cox, M.A.A., 2000. *Multidimensional scaling*. CRC press.

469 Domínguez, I., Doménech-Carbó, A., 2015. Screening and authentication of tea varieties  
470 based on microextraction-assisted voltammetry of microparticles. *Sensors Actuators B*  
471 *Chem.* 210, 491–499. <https://doi.org/https://doi.org/10.1016/j.snb.2015.01.009>

472 Edelman, G.J., Gaston, E., van Leeuwen, T.G., Cullen, P.J., Aalders, M.C.G., 2012.  
473 Hyperspectral imaging for non-contact analysis of forensic traces. *Forensic Sci. Int.* 223,  
474 28–39. <https://doi.org/https://doi.org/10.1016/j.forsciint.2012.09.012>

475 Fu, X., Ying, Y., 2016. Food Safety Evaluation Based on Near Infrared Spectroscopy and  
476 Imaging: A Review. *Crit. Rev. Food Sci. Nutr.* 56, 1913–1924.  
477 <https://doi.org/10.1080/10408398.2013.807418>

478 García Allende, P.B., Anabitarte García, F., Conde Portilla, O.M., Mirapeix Serrano,  
479 J.M., Madruga Saavedra, F.J., López Higuera, J.M., 2008. Support vector machines in

480 hyperspectral imaging spectroscopy with application to material identification. Proc.  
481 SPIE 6966, Algorithms and Technologies for Multispectral, Hyperspectral, and  
482 Ultraspectral Imagery XIV, 69661V. <http://dx.doi.org/10.1117/12.770306>

483 Garcia-Allende, P.B., Conde, O.M., Mirapeix, J., Cobo, A., Lopez-Higuera, J.M., 2008.  
484 Quality control of industrial processes by combining a hyperspectral sensor and Fisher's  
485 linear discriminant analysis. *Sensors Actuators B Chem.* 129, 977–984.  
486 <https://doi.org/https://doi.org/10.1016/j.snb.2007.09.036>

487 Goetz, A.F., Vane, G., Solomon, J.E., Rock, B.N., 1985. Imaging spectrometry for Earth  
488 remote sensing. *Science* 228, 1147–1153. <https://doi.org/10.1126/science.228.4704.1147>

489 He, Y., Li, X., Deng, X., 2007. Discrimination of varieties of tea using near infrared  
490 spectroscopy by principal component analysis and BP model. *J. Food Eng.* 79, 1238–  
491 1242. <https://doi.org/https://doi.org/10.1016/j.jfoodeng.2006.04.042>

492 Jing, J., Shi, Y., Zhang, Q., Wang, J., Ruan, J., 2017. Prediction of Chinese green tea  
493 ranking by metabolite profiling using ultra-performance liquid chromatography–  
494 quadrupole time-of-flight mass spectrometry (UPLC–Q-TOF/MS). *Food Chem.* 221,  
495 311–316. <https://doi.org/https://doi.org/10.1016/j.foodchem.2016.10.068>

496 Kandpal, L.M., Lohumi, S., Kim, M.S., Kang, J.-S., Cho, B.-K., 2016. Near-infrared  
497 hyperspectral imaging system coupled with multivariate methods to predict viability and  
498 vigor in muskmelon seeds. *Sensors Actuators B Chem.* 229, 534–544.  
499 <https://doi.org/https://doi.org/10.1016/j.snb.2016.02.015>



500 Kandpal, L.M., Tewari, J., Gopinathan, N., Boulas, P., Cho, B.-K., 2016. In-Process  
501 Control Assay of Pharmaceutical Microtablets Using Hyperspectral Imaging Coupled  
502 with Multivariate Analysis. *Anal. Chem.* 88, 11055–11061.  
503 <https://doi.org/10.1021/acs.analchem.6b02969>

504 Kumar, A.S., Shanmugam, R., Nellaiappan, S., Thangaraj, R., 2016. Tea quality  
505 assessment by analyzing key polyphenolic functional groups using flow injection analysis  
506 coupled with a dual electrochemical detector. *Sensors Actuators B Chem.* 227, 352–361.  
507 <https://doi.org/https://doi.org/10.1016/j.snb.2015.12.072>

508 Lee, M.-S., Hwang, Y.-S., Lee, J., Choung, M.-G., 2014. The characterization of caffeine  
509 and nine individual catechins in the leaves of green tea (*Camellia sinensis* L.) by near-  
510 infrared reflectance spectroscopy. *Food Chem.* 158, 351–357.  
511 <https://doi.org/10.1016/j.foodchem.2014.02.127>

512 Li, J., Fu, B., Huo, D., Hou, C., Yang, M., Shen, C., Luo, H., Yang, P., 2017.  
513 Discrimination of Chinese teas according to major amino acid composition by a  
514 colorimetric {IDA} sensor. *Sensors Actuators B Chem.* 240, 770–778.  
515 <https://doi.org/http://dx.doi.org/10.1016/j.snb.2016.09.019>

516 Lu, G., Fei, B., 2014. Medical hyperspectral imaging: a review. *J. Biomed. Opt.* 19,  
517 10901. <https://doi.org/10.1117/1.JBO.19.1.010901>

518 Lv, H., Zhang, Y., Lin, Z., Liang, Y., 2013. Processing and chemical constituents of Pu-  
519 erh tea: A review. *Food Res. Int.* 53, 608–618.  
520 <https://doi.org/https://doi.org/10.1016/j.foodres.2013.02.043>

521 Maaten, L. van der, Hinton, G., 2008. Visualizing high-dimensional data using t-SNE. J.  
522 Mach. Learn. Res. 9, 2579–2605.

523 Maaten, L. van der, Postma, E., Van den Herik, J., 2009. Dimensionality reduction: a  
524 comparative review. Tilburg University Technical Report, TICC-TR 2009-005.

525 Mahalanobis, P.C., 1936. On the generalised distance in statistics, in: Proceedings  
526 National Institute of Science, India. pp. 49–55.

527 Mishra, P., Asaari, M.S.M., Herrero-Langreo, A., Lohumi, S., Diezma, B., Scheunders,  
528 P., 2017. Close range hyperspectral imaging of plants: A review. Biosyst. Eng. 164, 49–  
529 67. <https://doi.org/https://doi.org/10.1016/j.biosystemseng.2017.09.009>

530 Mishra, P., Cordella, C.B.Y., Rutledge, D.N., Barreiro, P., Roger, J.M., Diezma, B.,  
531 2016. Application of independent components analysis with the JADE algorithm and NIR  
532 hyperspectral imaging for revealing food adulteration. J. Food Eng. 168, 7–15.

533 Mountrakis, G., Im, J., Ogole, C., 2011. Support vector machines in remote sensing: A  
534 review. ISPRS J. Photogramm. Remote Sens. 66, 247–259.  
535 <https://doi.org/https://doi.org/10.1016/j.isprsjprs.2010.11.001>

536 Nansen, C., Singh, K., Mian, A., Allison, B.J., Simmons, C.W., 2016. Using  
537 hyperspectral imaging to characterize consistency of coffee brands and their respective  
538 roasting classes. J. Food Eng. 190, 34–39.  
539 <https://doi.org/https://doi.org/10.1016/j.jfoodeng.2016.06.010>

540 Nieh, C.-H., Hsieh, B.-C., Chen, P.-C., Hsiao, H.-Y., Cheng, T.-J., Chen, R.L.C., 2009.  
541 Potentiometric flow-injection estimation of tea fermentation degree. *Sensors Actuators B*  
542 *Chem.* 136, 541–545. <https://doi.org/https://doi.org/10.1016/j.snb.2008.09.024>

543 Ozturk, B., Seyhan, F., Ozdemir, I.S., Karadeniz, B., Bahar, B., Ertas, E., Ilgaz, S., 2016.  
544 Change of enzyme activity and quality during the processing of Turkish green tea. *LWT -*  
545 *Food Sci. Technol.* 65, 318–324. <https://doi.org/https://doi.org/10.1016/j.lwt.2015.07.068>

546 Panigrahi, N., Bhol, C.S., Das, B.S., 2016. Rapid assessment of black tea quality using  
547 diffuse reflectance spectroscopy. *J. Food Eng.* 190, 101–108.  
548 <https://doi.org/https://doi.org/10.1016/j.jfoodeng.2016.06.020>

549 Plaza, A., Benediktsson, J.A., Boardman, J.W., Brazile, J., Bruzzone, L., Camps-Valls,  
550 G., Chanussot, J., Fauvel, M., Gamba, P., Gualtieri, A., Marconcini, M., Tilton, J.C.,  
551 Trianni, G., 2009. Recent advances in techniques for hyperspectral image processing.  
552 *Remote Sens. Environ.* 113, S110–S122.  
553 <https://doi.org/https://doi.org/10.1016/j.rse.2007.07.028>

554 Pu, Y.-Y., Feng, Y.-Z., Sun, D.-W., 2015. Recent Progress of Hyperspectral Imaging on  
555 Quality and Safety Inspection of Fruits and Vegetables: A Review. *Compr. Rev. Food*  
556 *Sci. Food Saf.* 14, 176–188. <https://doi.org/10.1111/1541-4337.12123>

557 Qu, J.-H., Liu, D., Cheng, J.-H., Sun, D.-W., Ma, J., Pu, H., Zeng, X.-A., 2015.  
558 Applications of Near-infrared Spectroscopy in Food Safety Evaluation and Control: A  
559 Review of Recent Research Advances. *Crit. Rev. Food Sci. Nutr.* 55, 1939–1954.  
560 <https://doi.org/10.1080/10408398.2013.871693>

561 Ruan, J., Haerdter, R., Gerendás, J., 2010. Impact of nitrogen supply on carbon/nitrogen  
562 allocation: a case study on amino acids and catechins in green tea [*Camellia sinensis* (L.)  
563 O. Kuntze] plants\*. *Plant Biol.* 12, 724–734. [https://doi.org/10.1111/j.1438-](https://doi.org/10.1111/j.1438-8677.2009.00288.x)  
564 [8677.2009.00288.x](https://doi.org/10.1111/j.1438-8677.2009.00288.x)

565 Sabale, S.P., Jadhav, C.R., 2015. Hyperspectral Image Classification Methods in Remote  
566 Sensing - A Review, in: 2015 International Conference on Computing Communication  
567 Control and Automation. pp. 679–683. <https://doi.org/10.1109/ICCUBEA.2015.139>

568 Sang, S., 2016. Tea: Chemistry and Processing BT - Encyclopedia of Food and Health.  
569 Academic Press, Oxford, pp. 268–272. [https://doi.org/https://doi.org/10.1016/B978-0-12-](https://doi.org/https://doi.org/10.1016/B978-0-12-384947-2.00685-1)  
570 [384947-2.00685-1](https://doi.org/https://doi.org/10.1016/B978-0-12-384947-2.00685-1)

571 Savitzky, A., Golay, M.J.E., 1964. Smoothing and Differentiation of Data by Simplified  
572 Least Squares Procedures. *Anal. Chem.* 36, 1627–1639.  
573 <https://doi.org/10.1021/ac60214a047>

574 Sharma, P., Ghosh, A., Tudu, B., Sabhapondit, S., Baruah, B.D., Tamuly, P.,  
575 Bhattacharyya, N., Bandyopadhyay, R., 2015. Monitoring the fermentation process of  
576 black tea using QCM sensor based electronic nose. *Sensors Actuators B Chem.* 219, 146–  
577 157. <https://doi.org/https://doi.org/10.1016/j.snb.2015.05.013>

578 Shrestha, S., Knapič, M., Žibrat, U., Deleuran, L.C., Gislum, R., 2016. Single seed near-  
579 infrared hyperspectral imaging in determining tomato (*Solanum lycopersicum* L.) seed  
580 quality in association with multivariate data analysis. *Sensors Actuators B Chem.* 237,  
581 1027–1034. <https://doi.org/https://doi.org/10.1016/j.snb.2016.08.170>

582 Tan, J., Dai, W., Lu, M., Lv, H., Guo, L., Zhang, Y., Zhu, Y., Peng, Q., Lin, Z., 2016.  
583 Study of the dynamic changes in the non-volatile chemical constituents of black tea  
584 during fermentation processing by a non-targeted metabolomics approach. *Food Res. Int.*  
585 79, 106–113. <https://doi.org/https://doi.org/10.1016/j.foodres.2015.11.018>

586 Tan, S.-M., Luo, R.-M., Zhou, Y.-P., Gong, H., Tan, Z., 2012. Rapid and non-destructive  
587 discrimination of tea varieties by near infrared diffuse reflection spectroscopy coupled  
588 with classification and regression trees. *African J. Biotechnol.* 11, 2303–2312.

589 Tenenbaum, J.B., 1998. Mapping a Manifold of Perceptual Observations, in: Jordan,  
590 M.I., Kearns, M.J., Solla, S.A. (Eds.), *Advances in Neural Information Processing*  
591 *Systems 10*. MIT Press, pp. 682–688.

592 Vapnik, V.N., Vapnik, V., 1998. *Statistical learning theory*. Wiley New York.

593 Wang, S., Yang, X., Zhang, Y., Phillips, P., Yang, J., Yuan, T.-F., 2015. Identification of  
594 Green, Oolong and Black Teas in China via Wavelet Packet Entropy and Fuzzy Support  
595 Vector Machine. *Entropy*. 17, 6663-6682. <https://doi.org/10.3390/e17106663>

596 Wang, X., Huang, J., Fan, W., Lu, H., 2015. Identification of green tea varieties and fast  
597 quantification of total polyphenols by near-infrared spectroscopy and ultraviolet-visible  
598 spectroscopy with chemometric algorithms. *Anal. Methods* 7, 787–792.  
599 <https://doi.org/10.1039/C4AY02106A>

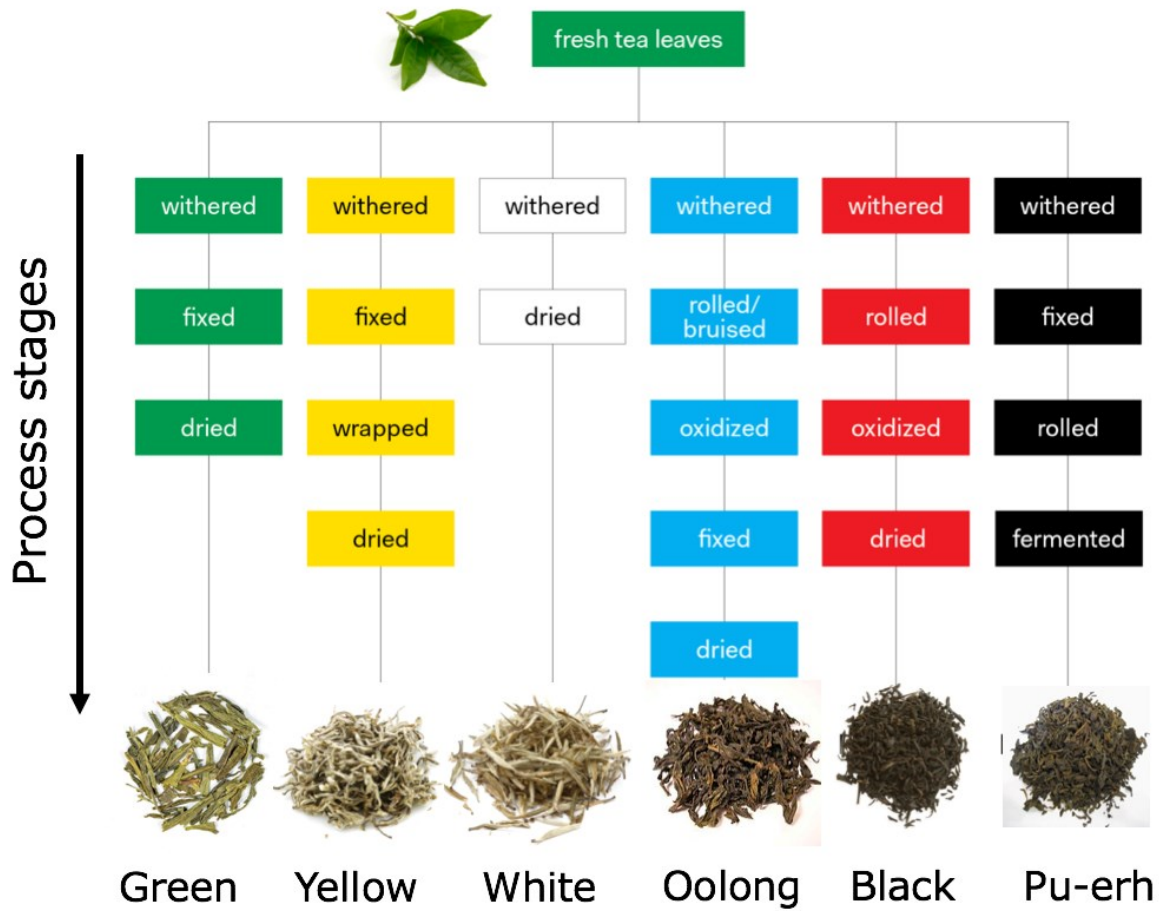
600 Wold, S., Esbensen, K., Geladi, P., 1987. Principal component analysis. *Chemom. Intell.*  
601 *Lab. Syst.* 2, 37–52. [https://doi.org/https://doi.org/10.1016/0169-7439\(87\)80084-9](https://doi.org/https://doi.org/10.1016/0169-7439(87)80084-9)

602 Xie, C., Li, X., Shao, Y., He, Y., 2015. Color Measurement of Tea Leaves at Different  
603 Drying Periods Using Hyperspectral Imaging Technique. PLoS One 9, 1–15.  
604 <https://doi.org/10.1371/journal.pone.0113422>

605 Yaroshenko, I., Kirsanov, D., Kartsova, L., Bhattacharyya, N., Sarkar, S., Legin, A.,  
606 2014. On the application of simple matrix methods for electronic tongue data processing:  
607 Case study with black tea samples. Sensors Actuators B Chem. 191, 67–74.  
608 <https://doi.org/https://doi.org/10.1016/j.snb.2013.09.093>

609 Zhao, J., Chen, Q., Cai, J., Ouyang, Q., 2009. Automated tea quality classification by  
610 hyperspectral imaging. Appl. Opt. 48, 3557–3564. <https://doi.org/10.1364/AO.48.003557>

611 Zhu, H., Ye, Y., He, H., Dong, C., 2017. Evaluation of green tea sensory quality via  
612 process characteristics and image information. Food Bioprod. Process. 102, 116–122.  
613 <https://doi.org/https://doi.org/10.1016/j.fbp.2016.12.004>



614

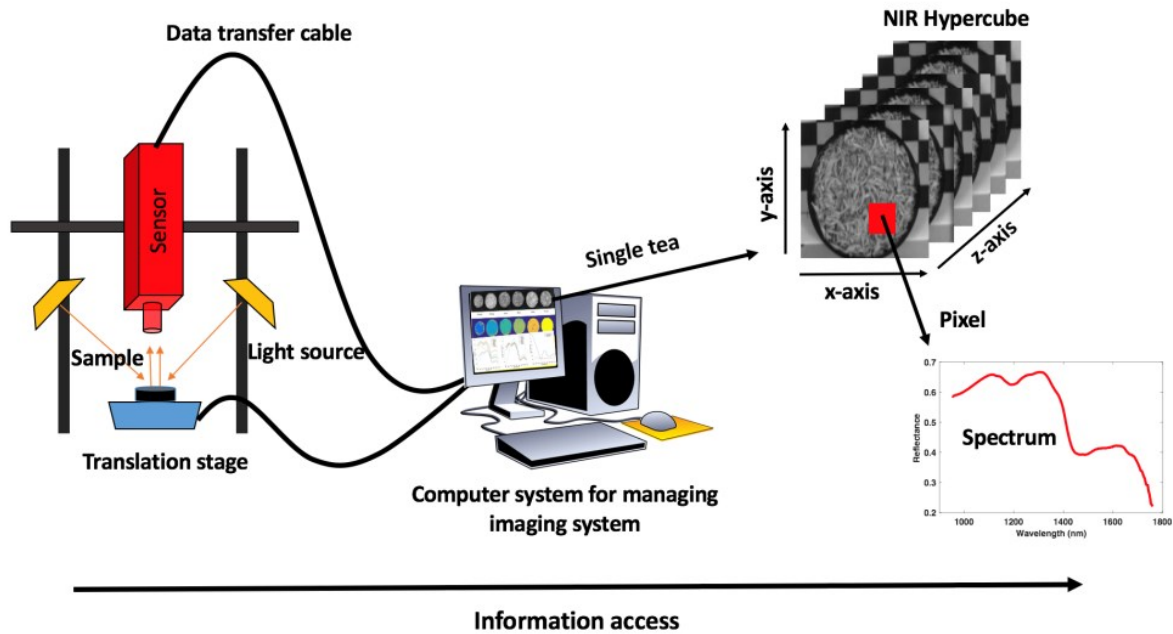
615 *Figure 2: Processing steps for different tea products starting from fresh green tea leaves to final*  
 616 *products.*

617

618

619

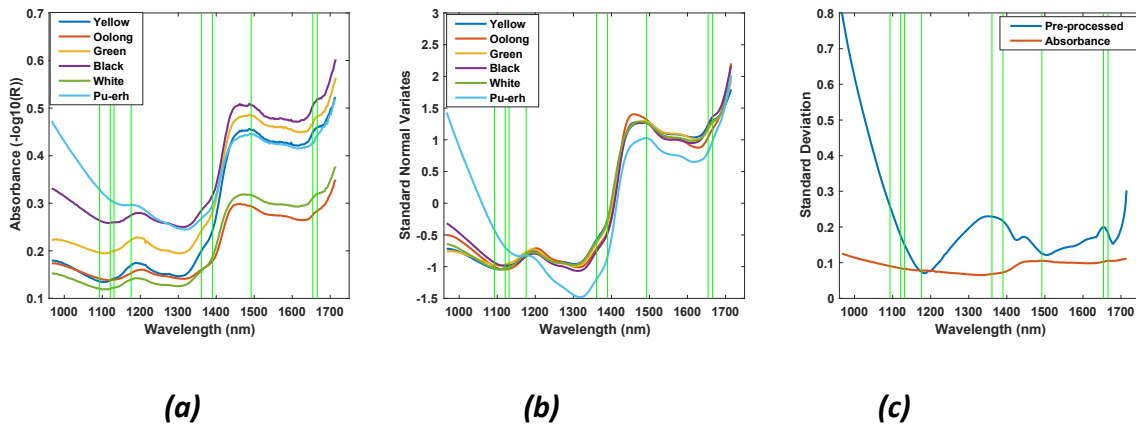
620



621

622 *Figure 2: Illustrative diagram for the hyperspectral imaging setup used to acquire the images of*  
 623 *tea samples.*

624



625

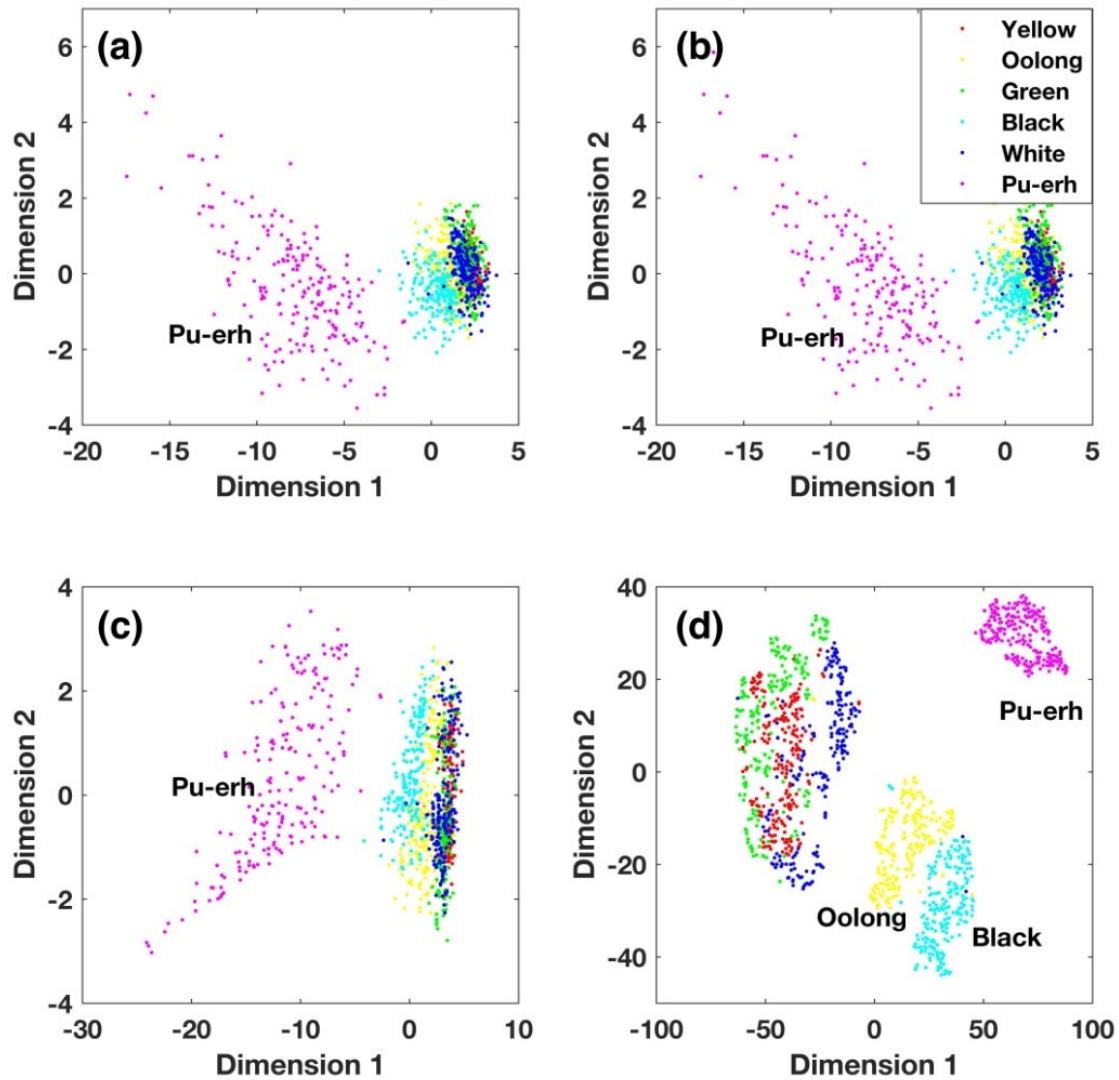
626

627 *Figure 3: Absorbance spectra of pure tea samples of yellow, oolong, green, black, white and Pu-*  
 628 *erh. (a). Mean absorbance spectra ( $n = 200$ ). (b) Mean spectra after pre-processing (SNV and*  
 629 *Savitzky- Golay smoothing), and (c) standard deviation of the absorbance spectra and spectra*  
 630 *after pre- processing. The vertical green lines denote the positions of the main peaks.*

631

632

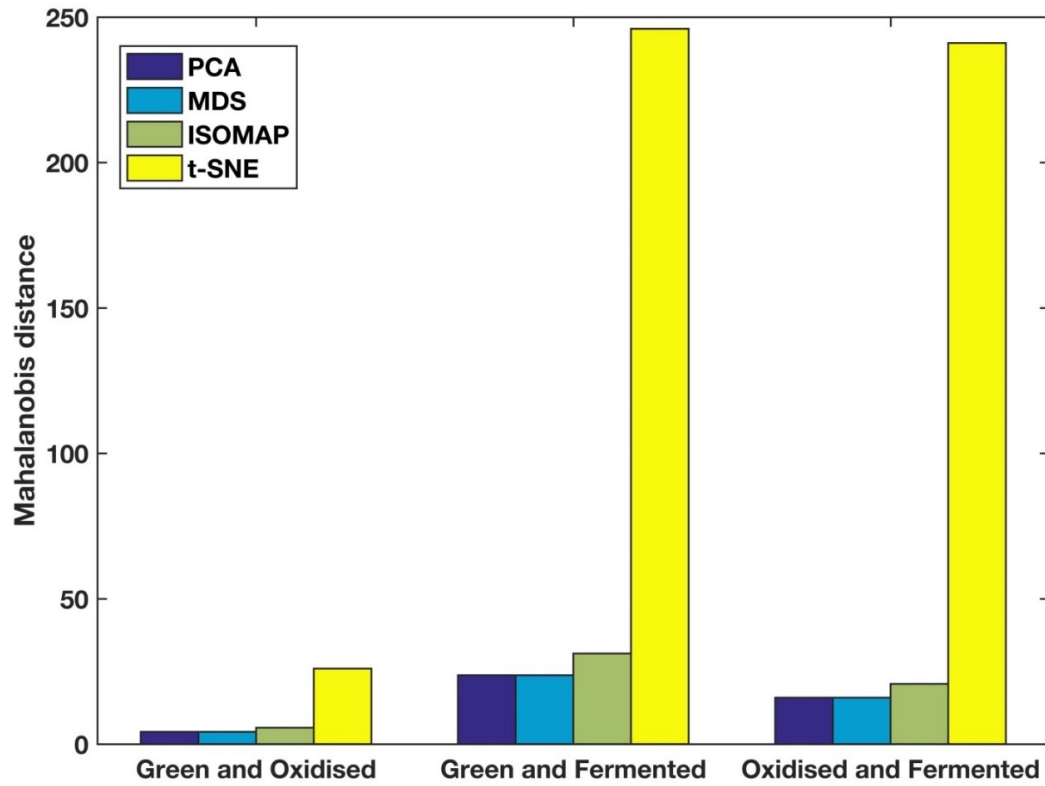




633

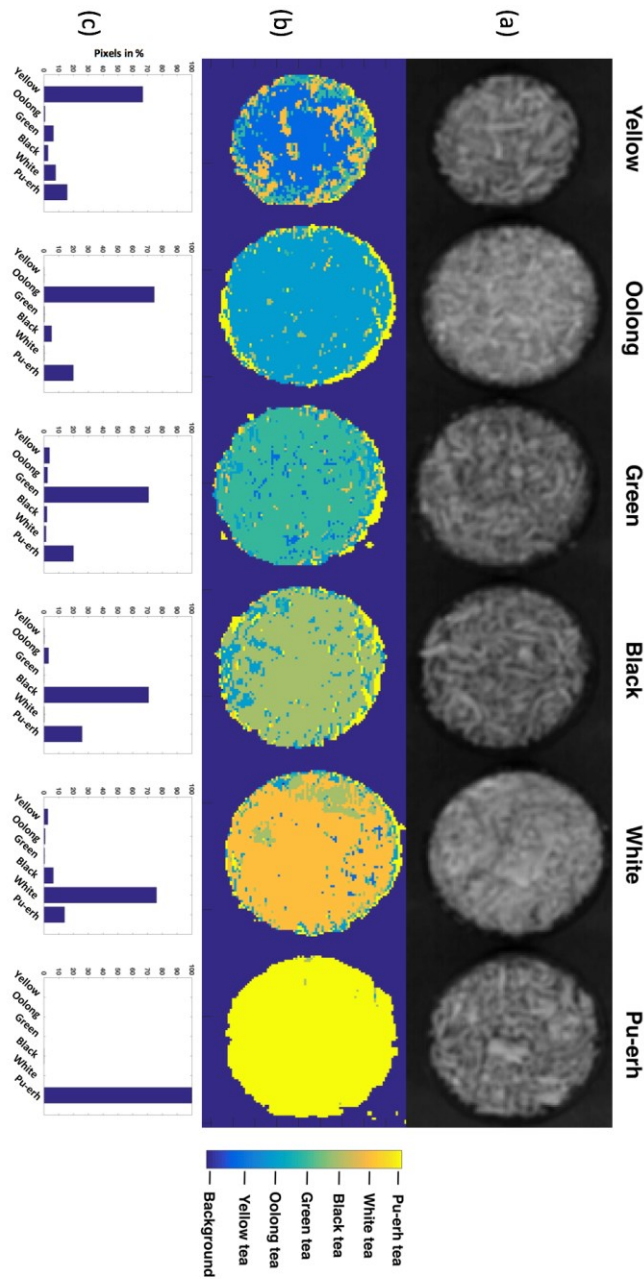
634 *Figure 4: 2-Dimensional scatter plots for visualising high dimensional tea data. (a).*  
 635 *Principal Component Analysis (PCA), (b). Multidimensional Scaling (MDS), (c). Isometric*  
 636 *Mapping (ISOMAP), and (d). t-distributed Stochastic Neighbour Embedding (t-SNE). In all the*  
 637 *plots, the first dimension is represented in the x-axis and the second in the y-axis, and the six tea*  
 638 *products are coloured as follows: Pu-erh (pink), black (sky blue), oolong (yellow), green (green),*  
 639 *white (blue) and yellow (red).*

640



641

642 *Figure 5: Mahalanobis distances between the three different cluster groups obtained using PCA*  
 643 *(dark-blue), MDS (sky-blue), ISOMAP (light- green) and t-SNE (yellow).*

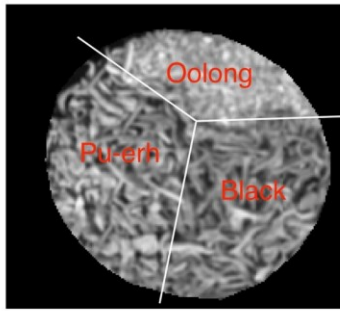


644

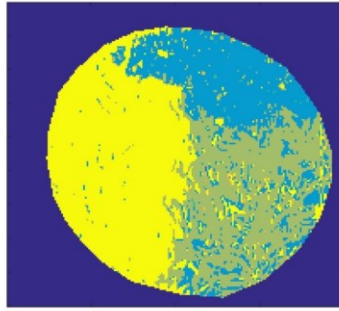
645 *Figure 6: (a) Greyscale image constructed from the spectral plane extracted from the hypercube*  
 646 *at 1424 nm, (b) Classification maps obtained from the application of the ECOC-SVM model. From*  
 647 *left to right the samples can be understood as yellow (dark blue), oolong (light blue), green (cyan),*  
 648 *black (light green), white (orange) and Pu-erh (yellow). (c) Histograms showing the proportion of*  
 649 *pixels attributed to the different tea products for the classification maps in (b).*

650

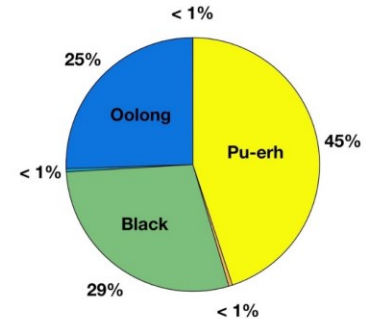
651



a.

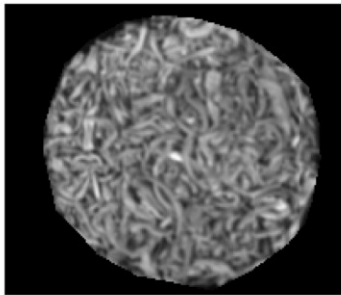


b.

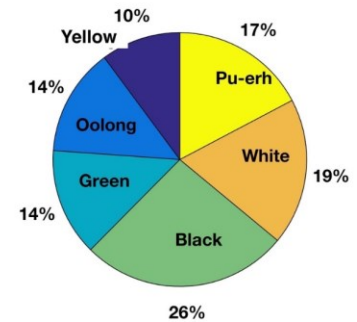
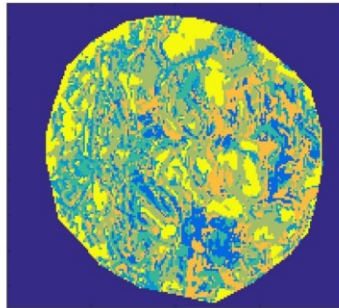


c.

d.



e.



f.

652

653 *Figure 7: (a). Greyscale image at 1424 nm for the sample comprising oolong, black and Pu-erh*  
 654 *tea, (b). The classification map for the sample comprising oolong, black and Pu-erh tea, (c). Pie*  
 655 *chart representing the proportion of pixels belonging to a particular class for the classification*  
 656 *map presented in (b), (d). Greyscale image at 1424 nm for a sample containing a mixture of all*  
 657 *teas, (e). The classification map for a sample containing a mixture of all teas, and (f) Pie chart*  
 658 *representing the proportion of pixels belonging to a particular class for the classification map*  
 659 *presented in (e).*

660

661